ARTICLES
https://doi.org/10.1038/s41477-018-0348-x

nature plants

Noncanonical ATG8–ABS3 interaction controls senescence in plants

Min Jia[1,5], Xiayan Liu[1,5], Hui Xue[1], Yue Wu[2,3], Lin Shi[2,3], Rui Wang[1,4], Yu Chen[1], Ni Xu[1], Jun Zhao[1], Jingxia Shao[1], Yafei Qi[1], Lijun An[1], Jen Sheen[2,3] and Fei Yu[1*]

Protein homeostasis is essential for cellular functions and longevity, and the loss of proteostasis is one of the hallmarks of senescence. Autophagy is an evolutionarily conserved cellular degradation pathway that is critical for the maintenance of proteostasis. Paradoxically, autophagy deficiency leads to accelerated protein loss by unknown mechanisms. We discover that the ABNORMAL SHOOT3 (ABS3) subfamily of multidrug and toxic compound extrusion transporters promote senescence under natural and carbon-deprivation conditions in *Arabidopsis thaliana*. The senescence-promoting ABS3 pathway functions in parallel with the longevity-promoting autophagy to balance plant senescence and survival. Surprisingly, ABS3 subfamily multidrug and toxic compound extrusion proteins interact with AUTOPHAGY-RELATED PROTEIN 8 (ATG8) at the late endosome to promote senescence and protein degradation without canonical cleavage and lipidation of ATG8. This non-autophagic ATG8–ABS3 interaction paradigm is probably conserved among dicots and monocots. Our findings uncover a previously unknown non-autophagic function of ATG8 and an unrecognized senescence regulatory pathway controlled by ATG8–ABS3-mediated proteostasis.

From ancient tonics to modern molecular interventions, the quest for longevity has always been part of human nature. Nutrient availability is closely tied with growth and longevity in many organisms[1]. In higher plants, the manipulations of nutrient availability, such as the deprivation of carbon or nitrogen sources, can also modulate plant senescence[2,3]. In addition, many key regulators of senescence are conserved in plants, suggesting that the regulation of longevity may be conserved in eukaryotic systems[1,4–7]. Consistent with this notion, over-expressions of *KIN10* and *KIN11*, encoding plant homologues of 5′ AMP-activated protein kinase, promote plant longevity in *Arabidopsis*[7].

Despite the tremendous progress in understanding the control of life span and senescence in yeast and model animals, much less is known mechanistically in higher plants. During senescence, nutrients are mobilized and reallocated to the sink organs (especially seeds), to ensure the reproductive success of plants[8–11]. The proper elaboration of plant senescence is modulated by internal developmental and hormonal signals[10,11]. In addition, external environmental conditions, including both biotic and abiotic stresses, can also trigger premature plant senescence[12,13].

Autophagy is responsible for the delivery of cellular components to the lysosome/vacuole for degradation, especially under nutrient limitation as well as other stress conditions, and is essential for cellular proteostasis and longevity[14]. The canonical autophagy pathway, culminating in the formation of phosphatidylethanolamine-conjugated AUTOPHAGY-RELATED PROTEIN 8 (ATG8-PE) and autophagosome, is highly conserved among eukaryotes including higher plants[3,15]. The hallmark phenotype of plant autophagy mutants is paradoxically an accelerated loss of bulk cellular proteins, especially chloroplast proteins, which account for about 80% of total leaf nitrogen, during natural or nutrient-deprivation-induced senescence[2,3,16,17]. This intriguing yet unexplained phenotype of plant *atg* mutants suggests that additional catabolic pathway(s) are operating in the absence of autophagy.

Multidrug and toxic compound extrusion (MATE) family transporters are multidrug efflux carriers and are ubiquitously present in prokaryotic and eukaryotic organisms[18]. In bacteria, MATE is involved in the export of a plethora of xenobiotic compounds including antibiotics[18]. In budding yeast, a MATE protein, YHR032W, was shown to mediate longevity, through modulation of *S*-adenosyl-L-methionine levels and activation of 5′ AMP-activated protein kinase[19]. In humans, two plasma-membrane-localized MATEs are responsible for the extrusion of a diverse spectrum of cationic drugs[20]. Surprisingly, the MATE transporter family has expanded dramatically in higher plants, and at least 56 putative members have been identified in *Arabidopsis*[21]. Plant MATEs have been shown to reside on various cellular membranes, including the plasma membrane, chloroplast envelope, endosomal membrane and tonoplast, and are involved in a diverse array of physiological activities[21–32].

We are interested in elucidating the mechanisms of plant senescence. Previously, we showed that ectopic expression of two *Arabidopsis* MATE family genes, *ABS3* and *ABS4*, in the gain-of-function mutants *abs3-1 dominant (1D)* and *abs4-1D* leads to sucrose-dependent cell elongation defects[30]. We observed empirically that adult *abs3-1D* and *abs4-1D* plants exhibited precocious senescence, and hypothesized that the actin binding site 3 transporter (ABS3) and its close homologues may modulate senescence in *Arabidopsis*. In this study, we establish a molecular framework of a previously unknown senescence regulatory pathway mediated by the ABS3 subfamily MATE proteins in higher plants. Interestingly, the ABS3-mediated senescence pathway necessitates physical interaction between ABS3 and ATG8 at the late endosome, but does not require ATG8-PE conjugation or ATG5/7-dependent canonical autophagy. Moreover, this senescence pathway controlled by the

[1]State Key Laboratory of Crop Stress Biology for Arid Areas and College of Life Sciences, Northwest A&F University, Yangling, Shaanxi, China. [2]Department of Molecular Biology and Centre for Computational and Integrative Biology, Massachusetts General Hospital, Boston, MA, USA. [3]Department of Genetics, Harvard Medical School, Boston, MA, USA. [4]Present address: Department of Molecular Genetics, Center for Applied Plant Science, Ohio State University, Columbus, OH, USA. [5]These authors contributed equally: Min Jia, Xiayan Liu. *e-mail: flyfeiyu@gmail.com

ATG8–ABS3 interaction is probably conserved among dicots and monocots. Taken together, our findings uncover a novel function of ATG8 distinct from its canonical role in autophagy, and also discover an evolutionarily conserved mechanism that controls senescence in higher plants.

Results

ABS3 subfamily MATE transporters promote senescence in *Arabidopsis*. To screen for new components of the plant senescence pathway, we established a robust assay to monitor the senescence process of *Arabidopsis* seedlings on carbon deprivation (Supplementary Fig. 1a). When light-grown 7-day-old wild type (WT) seedlings were transferred to medium lacking exogenous sugar and placed in the dark, senescence was induced, as indicated by the rapid reduction of chlorophyll and the degradation of cellular proteins (Supplementary Fig. 1b–d). Utilizing this assay, we tested the carbon deprivation responses of *abs3-1D*, an activation tagged gain-of-function mutant that shows precocious senescence in adult plants[30]. Compared with the WT, *abs3-1D* showed greatly accelerated senescence on carbon deprivation (Fig. 1a). ABS3 belongs to the MATE transporter family (Supplementary Fig. 1e)[21]. Five additional MATE proteins are closely related to ABS3 in the same phylogenetic clade that we designated the ABS3 subfamily (Fig. 1b and Supplementary Fig. 1e). *abs4-1D*, a gain-of-function allele of *ABS4*, also showed accelerated senescence under carbon deprivation (Supplementary Fig. 1f)[30]. To test whether ABS3 subfamily MATEs share redundant functions in carbon-deprivation-induced senescence, we examined the responses of individual loss-of-function MATE family mutants. Among six single MATE family mutants, only *abs3-1* and *abs3l2-1* showed slightly delayed senescence while the progression of senescence in the other four MATE family mutants was comparable to that of the WT (Fig. 1c and Supplementary Fig. 1g). Next, we analysed carbon-deprivation-induced senescence in higher-order MATE family mutants. A trend of increased degrees of delayed senescence was observed in the double-mutant *mated* (*abs3-1 abs4-1*), quadruple-mutant *mateq* (*abs3-1 abs4-1 abs3l1-1 abs3l2-1*) and sextuple-mutant *mates* (*abs3-1 abs4-1 abs3l1-1 abs3l2-1 abs3l3-1 abs3l4-1*) (Fig. 1d).

Since *mateq* showed a pronounced delay of senescence, most analyses were performed with *mateq* in this study. Next, we carried out in-depth characterizations of carbon deprivation responses in the WT, *abs3-1D* and *mateq*. Quantitative analyses showed that chlorophyll reduction and total cellular protein reduction on a fresh tissue weight basis were faster in *abs3-1D* than in the WT, but were greatly delayed in *mateq* (Fig. 1e). Coomassie Brilliant Blue (CBB)-stained protein gel and immunoblotting of the rubisco large subunit (RBCL) showed that reductions of bulk cellular protein and RBCL were hastened in *abs3-1D* and were significantly delayed in *mateq* compared with the WT (Fig. 1f). As expected, carbon deprivation effectively induced accumulation of the autophagy marker ATG8-PE (Fig. 1f). At the transcript level, the onset of senescence activates senescence-associated genes and represses photosynthesis-related genes. Compared with the WT, a more acute induction of the senescence marker genes *SAG12*, *ORE1* and *SGR1* was observed in *abs3-1D*, while in *mateq* the inductions were greatly attenuated (Fig. 1g)[33,34]. Similarly, the repression of genes encoding components of the photosynthetic electron transport chain (*CAB3* and *PetC*) and a subunit of the chloroplast ribosome (*PRPL13*) was stronger in *abs3-1D* but weaker in *mateq* compared with gene expression in the WT (Fig. 1g). In addition to carbon deprivation, ABS3 subfamily MATEs also promote senescence under nitrogen starvation (Supplementary Fig. 1h), suggesting that they may have a broader role in regulating the nutrient stress responses.

In plants, natural and stress-induced senescence are overlapping but distinct processes[11,12]. To determine whether ABS3 subfamily MATEs play a role in natural senescence, we monitored the natural senescence process in the WT, *abs3-1D* and *mateq*. At 16 d old, the first pair of true leaves had comparable levels of total cellular protein in all three genotypes (Fig. 1h,i). However, the first pair of true leaves of 26-d-old *abs3-1D* showed prominent signs of senescence, accompanied by a massive loss of cellular proteins and chlorophyll, while leaf chlorosis and the reduction in protein content were milder in *mateq* compared with in the WT (Fig. 1h,i). Importantly, the endogenous promoter-driven ABS3 and green fluorecent protein (*ABS3-GFP*) fusion gene (*pABS3:ABS3-GFP*) was sufficient to complement the delayed senescence phenotype in *mateq* and *mates*, respectively (Fig. 1j). Together, these data demonstrate that ABS3 subfamily MATEs are positive regulators for both carbon-deprivation-induced and natural developmental senescence.

ABS3 subfamily MATEs control senescence and proteostasis independent of canonical autophagy. The accelerated senescence phenotypes of *abs3-1D* and *abs4-1D* under carbon deprivation are reminiscent of plant *atg* mutants (Supplementary Fig. 2a)[35–38]. To probe the relationship between the ABS3-mediated pathway and autophagy, we first took a genetic approach and generated higher-order mutants of *ATG5*/*7* and *ABS3* subfamily MATE genes. Remarkably, the senescence phenotype of *atg7-3* under carbon deprivation was effectively suppressed in the *mateq atg7-3* mutant, suggesting a previously unknown role of ABS3 subfamily MATE proteins in regulating senescence in the absence of canonical autophagy (Fig. 2a). Consistently, the *abs3-1D atg7-3* double mutant was extremely sensitive to carbon deprivation, showing far more severe chlorosis (Fig. 2a). Analyses of the quintuple mutant *mateq atg5-1* and double mutant *abs3-1D atg5-1* corroborated the observations of the *mateq atg7-3* and *abs3-1D atg7-3*, respectively (Supplementary Fig. 2b). The reversal of early senescence phenotypes of *atg7-3* and *atg5-1* by *mateq* could bypass the need for autophagy to prevent senescence in plants. These findings suggest that the activities of the ABS3 subfamily MATEs act as a molecular switch for the senescence programme, regardless of whether canonical autophagy is functional.

To understand the molecular basis of these genetic interactions, we analysed the accumulations of ATG8 and ATG8-PE in these mutants. Consistent with the established functions of ATG5 and ATG7, on carbon deprivation, *atg7-3* or *atg5-1* failed to produce ATG8-PE, but accumulated high levels of ATG8 precursors, including a distinct ATG8 form that is not found in the WT (Fig. 2b and Supplementary Fig. 2c,d). Despite the opposite senescence phenotypes, *mateq atg7-3* and *abs3-1D atg7-3* showed ATG8 accumulation patterns similar to that of *atg7-3* (Fig. 2b). In addition, regardless of the carbon deprivation treatment, the degradation of NEIGHBOR OF BRCA1 (NBR1)—a cargo receptor and substrate for selective autophagy[39]—was only blocked when *ATG5* or *ATG7* was mutated, but was not affected in either *abs3-1D* or *mateq* (Fig. 2c). These results suggest that the flux of autophagy is uninterrupted in *abs3-1D* or *mateq*. Importantly, introducing *mateq* to the *atg7-3* or *atg5-1* background markedly slowed down the protein loss during carbon deprivation (Fig. 2b and Supplementary Fig. 2d). Meanwhile, adding the *abs3-1D* mutation to *atg7-3* or *atg5-1* further escalated the rate of protein loss (Fig. 2b and Supplementary Fig. 2c). Together, our genetic, biochemical and molecular evidence suggests that ABS3 subfamily MATEs control senescence and proteostasis independent of autophagy.

In *Arabidopsis*, the late endosome, multivesicular bodies and prevacuole are indistinguishable endomembrane compartments controlling the selective trafficking of proteins to the vacuole for degradation[40]. Previously, we showed that ABS3, ABS4, ABS3L1 and ABS3L2 co-localized with a late endosomal protein, SYP21 (ref. [30]). Next, we validated whether all six members of the ABS3 subfamily MATEs reside at the late endosome. When co-expressed in *Arabidopsis* leaf protoplasts, MATE-GFPs largely overlapped with

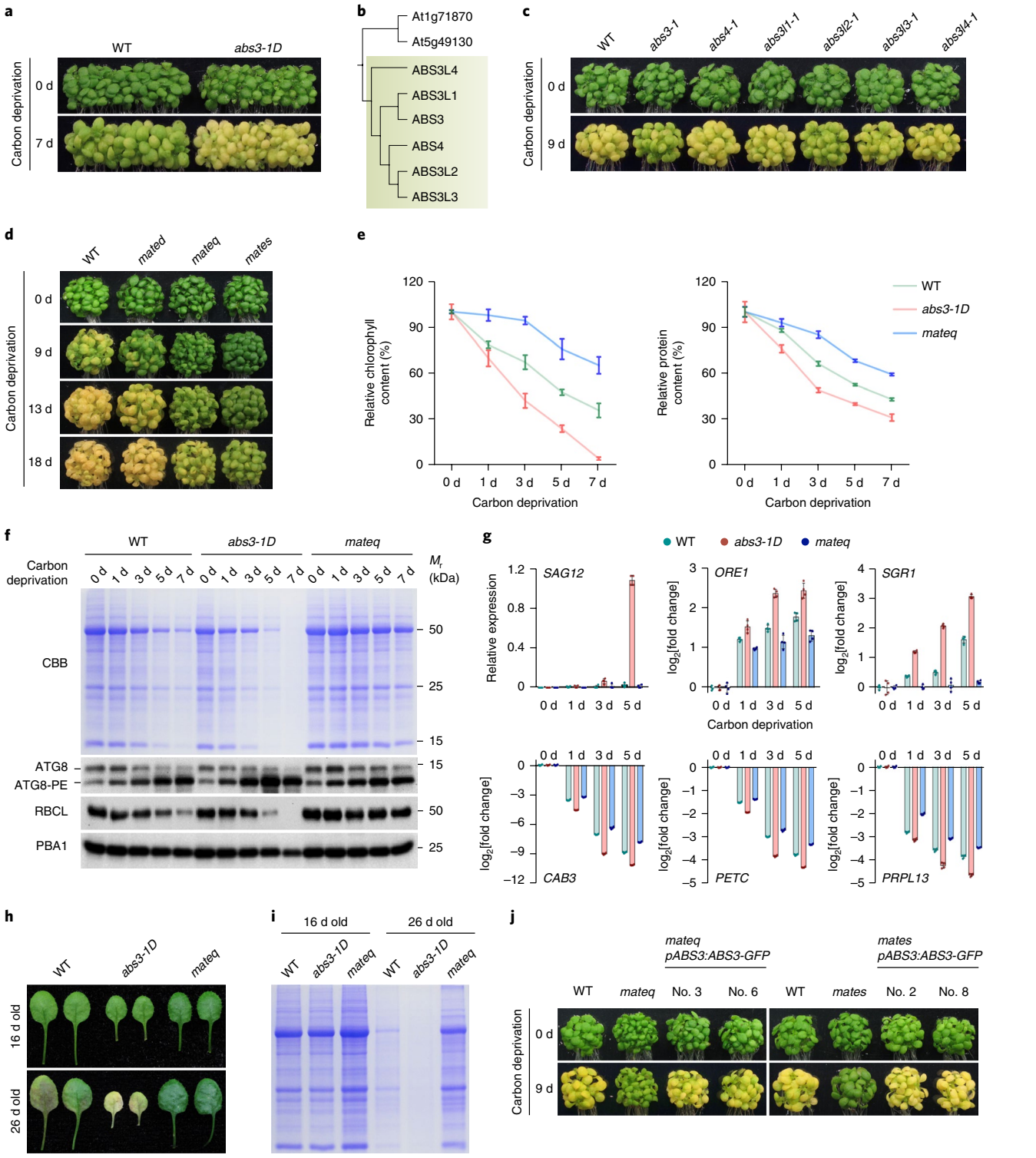

Fig. 1 | ABS3 subfamily MATEs promote plant senescence. a, Senescence phenotypes of the WT and *abs3-1D* before and after 7 d of carbon deprivation. **b**, The phylogenetic clade consists of ABS3 subfamily MATE proteins (shaded part). **c**, Senescence phenotypes of WT and single mutants of ABS3 subfamily MATE genes before and after 9 d of carbon deprivation. **d**, Senescence phenotypes of the WT, *mated* (*abs3-1abs4-1*), *mateq* (*abs3-1abs4-1abs3l1-1abs3l2-1*) and *mates* (*abs3-1abs4-1abs3l1-1abs3l2-1abs3l3-1abs3l4-1*) before and after 9, 13 and 18 d of carbon deprivation. **e**, Chlorophyll and protein content (normalized to equal amounts of fresh weight) reduction in the WT, *abs3-1D* and *mateq* during carbon deprivation. Data are presented as means ± s.d. ($n = 3$ biological replicates). **f**, Total cellular proteins from the WT, *abs3-1D* and *mateq* during carbon deprivation were resolved on SDS-PAGE, stained with CBB or probed with the indicated antibodies. anti-PBA1 served as a loading control. **g**, RT-qPCR analyses of the indicated genes in the WT, *abs3-1D* and *mateq* during carbon deprivation. The relative expression is shown for *SAG12*. The $\log_2$[fold change] with respect to the expression levels in the WT at 0 d is shown for the other genes. Data are presented as means ± s.d. ($n = 4$ biological replicates). **h**, First pairs of true leaves from 16- and 26-day-old WT, *abs3-1D* and *mateq*. **i**, The total cellular proteins in leaves shown in **h** were resolved on SDS-PAGE and stained with CBB. **j**, Complementation of *mateq* and *mates* by the expression of *pABS3:ABS3-GFP*. The experiments in **a**, **c**, **d**, **f** and **h**–**j** were repeated independently three times with similar results.

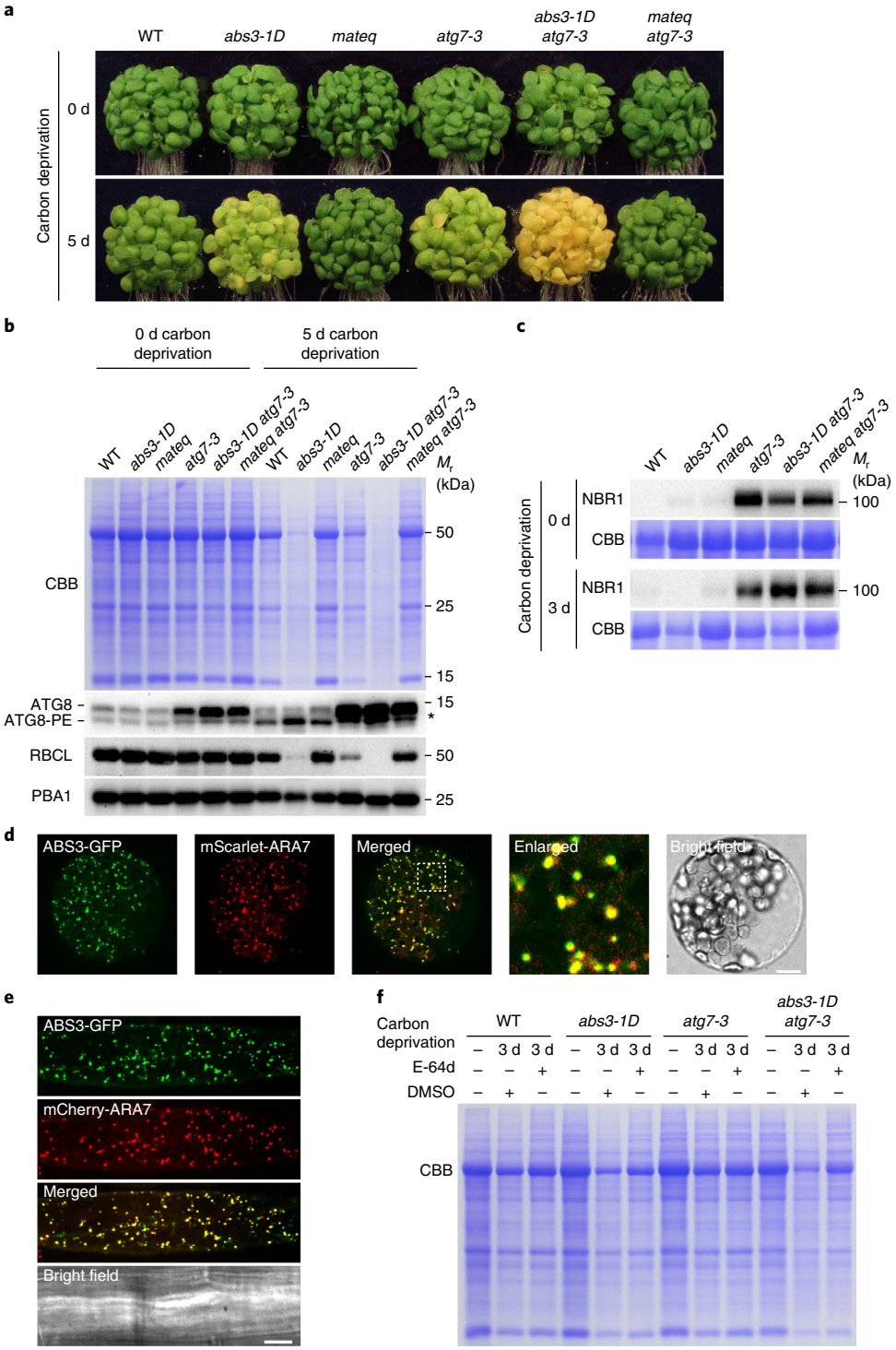

Fig. 2 | Genetic interaction between *abs3-1D*, *mateq* and the autophagy mutant *atg7-3*. **a**, Senescence phenotypes of the WT, *abs3-1D*, *mateq*, *atg7-3*, the *abs3-1D atg7-3* double mutant and the *mateq atg7-3* quintuple mutant before and after 5 d of carbon deprivation. **b**, Total cellular proteins from plants of the indicated genotypes before and after 5 d of carbon deprivation were resolved on SDS-PAGE, probed with the indicated antibodies or stained with CBB. The asterisk indicates a distinct ATG8 precursor or modification found in autophagy deficiency backgrounds. **c**, Immunoblot analysis of NBR1 accumulation in plants of the indicated genotypes before and after 3 d of carbon deprivation. **d**, Co-localization of ABS3-GFP and the late endosomal marker mScarlet-ARA7 in *Arabidopsis* leaf protoplasts. Scale bar, 10 μm. **e**, Root epidermal cells of the *Arabidopsis* transgenic line expressing both ABS3-GFP and mCherry-ARA7. Scale bar, 10 μm. **f**, Effects of E-64d on bulk protein reduction in the WT, *abs3-1D atg7-3* and *abs3-1D atg7-3* after 3 d of carbon deprivation. The experiments in **a**–**f** were repeated independently three times with similar results.

the late endosomal protein marker mScarlet-ARA7 (Fig. 2d and Supplementary Fig. 2e)[41,42]. Furthermore, in planta co-localizations of ABS3-GFP and mCherry-ARA7 were observed in the root epidermal cells of dual-labelling transgenic lines expressing both *p35S:ABS3-GFP* and *pUBQ10:mCherry-ARA7* (Fig. 2e). Next, we treated the transgenic plants *p35S:ABS3-GFP* and *pUBQ10:yellow*

fluorescent protein (YFP)-ARA7 with wortmannin—a phosphoinositide 3-kinase inhibitor known to cause the swelling of multivesicular bodies[40]. Both ABS3-GFP and YFP-ARA7 gave ring-like signals on wortmannin treatment (Supplementary Fig. 2f). The majority of ABS3-GFP signals were found on the periphery of the rings (probably the late endosomal delimiting membrane) and a minor portion of ABS3-GFP signals were also present inside the rings (Supplementary Fig. 2f,g).

Finally, we tested whether the proper function of the vacuole is required for ABS3-mediated proteostasis. An estimation of vacuolar cathepsin B-like cysteine protease activity by Magic Red Cathepsin B reagent staining suggested that cathepsin B-like protease activity is higher in *abs3-1D* than in the WT or *mateq* (Supplementary Fig. 2h,i). In addition, when the WT, *atg7-3, abs3-1D* and *abs3-1D atg7-3* seedlings were subjected to carbon deprivation and treated with E-64d (a vacuolar cysteine protease inhibitor), E-64d effectively impeded the rate of bulk protein reduction in *atg7-3, abs3-1D* and *abs3-1D atg7-3* seedlings after 3 d of carbon deprivation (Fig. 2f). These findings suggest that the ABS3-mediated catabolic pathway is at least partially dependent on the proteolytic activity of the vacuole.

ABS3 subfamily MATEs are novel ATG8-interacting partners at the late endosome. The hyperaccumulation of carbon-deprivation-induced ATG8-PE in *abs3-1D* implies a potential functional link between ABS3 and ATG8. To test this hypothesis, we assessed whether ABS3 physically interacts with ATG8. First, partial co-localization was observed in *Arabidopsis* leaf protoplasts co-expressing mCherry-ABS3 and GFP-ATG8e (Fig. 3a). Next, we probed the potential direct interaction between ABS3 and ATG8 by bimolecular fluorescence complementation (BiFC) assay in protoplasts and the split-ubiquitin assay in yeast[43,44]. In the BiFC assay, co-expressing amino (N)-terminal YFP-ABS3 (YN-ABS3) and carboxy (C)-terminal YFP-ATG8e (YC-ATG8e), but not YN-ABS3 and YC vector or YN vector and YC-ATG8e, in protoplasts reconstituted punctuated YFP signals that localized to mScarlet-ARA7-labelled late endosomes (Fig. 3b and Supplementary Fig. 3a). In the split-ubiquitin assay, the interaction of ABS3 or ABS4 with ATG8e activated the expression of reporter genes (Fig. 3c and Supplementary Fig. 3b). To expand our findings, we investigated the interactions between the other five members of the ABS3 subfamily and ATG8e with the BiFC assay, and showed that they interact at late endosomes (Supplementary Fig. 3c). We also confirmed that all nine *Arabidopsis* ATG8s (ATG8a–ATG8i) could interact with ABS3 subfamily MATEs (Supplementary Fig. 4). Lastly, we carried out a pull-down assay using purified recombinant glutathione S-transferase (GST)-ATG8e. GST-ATG8e, but not GST, was able to pull down ABS3-GFP from membrane fractions of *p35S:ABS3-GFP* transgenic lines (Fig. 3d). Together, our data support a direct physical interaction between ABS3 and ATG8 at the late endosome.

ATG8–ABS3 interaction is uncoupled from ABS3 transporter activity or the autophagic function of ATG8. The unexpected interaction between ABS3 and ATG8 prompted us to test whether ABS3 has acquired additional functions that could be uncoupled from its MATE transporter activity. To test this possibility, we first compared the amino acid sequences of the ABS3 subfamily MATEs with the MATE transporter of the hyperthermophilic archaeon *Pyrococcus furiosus* (PfMATE) and an *Arabidopsis* MATE AtDTX14, whose crystal structures and essential amino acids for transporter activity have been determined[45,46]. We identified Pro 66 in ABS3 as a conserved residue, whose corresponding residues in PfMATE and AtDTX14 (Pro 26 in PfMATE and Pro 36 in AtDTX1) are indispensable for their transporter activity (Fig. 4a). Converting Pro 66 to alanine in ABS3 would produce a presumably transporter-dead version of ABS3. Indeed, ABS3^{P66A} failed to complement the *Escherichia. coli* transporter mutant Δ*acrB*, as expressing ABS3, but not ABS3^{P66A}, conferred resistance to the antibiotic norfloxacin in the Δ*acrB* background (Fig. 4b). Co-expressions of GFP-ABS3^{P66A} with mCherry-ABS3 or mScarlet-ARA7 showed nicely overlapping signals, suggesting that the P66A mutation does not alter the subcellular localization of ABS3 (Supplementary Fig. 5a). Next, we checked the interactions between YN-ABS3^{P66A} and YC-ATG8e via BiFC assay in protoplasts, and found that the P66A mutation did not hamper the efficiency or localization of the reconstituted YFP signals (Fig. 4c and Supplementary Fig. 5b,f). Moreover, *Arabidopsis* transgenic lines expressing *p35S:ABS3^{P66A}* not only hastened senescence under carbon deprivation but also resembled *abs3-1D* when grown on soil (Fig. 4d,e and Supplementary Fig. 5g). Together, these results indicate that the ATG8–ABS3 interaction, as well as the regulation of senescence by ABS3, can be uncoupled from the transporter function of ABS3.

In canonical autophagy, ATG8 is processed by ATG4 at a conserved C-terminal glycine, and a ubiquitin-like conjugation system (ATG7 as E1; ATG3 as E2; ATG12-ATG5-ATG16 as E3) facilitates the formation of ATG8-PE moieties[3,15]. However, our genetic evidence suggests that the ABS3-mediated senescence pathway does not rely on ATG5 or ATG7, raising the question of whether the ATG8–ABS3 interaction requires the lipidation of ATG8. To test this, we first determined that Gly 118 of *Arabidopsis* ATG8e is the conserved glycine (Fig. 4f). YFP signals reconstituted by Gly 118-mutated YC-ATG8e^{G118A} and YN-ABS3 were indistinguishable from those produced by WT YC-ATG8e and YN-ABS3 (Fig. 4g and Supplementary Fig. 5c,f), suggesting that the formation of ATG8-PE is not necessary for ATG8–ABS3 interaction at the late endosome. Furthermore, BiFC assays of YC-ATG8e and YN-ABS3 carried out in *atg7-3* and *atg5-1* mutant protoplasts also yielded punctuated signals at late endosomes despite the blockage of autophagy and ATG8-PE conjugation (Fig. 4h,i and Supplementary Fig. 5d–f). These data suggest that ABS3 could recruit unconjugated ATG8 to the late endosome, and also indicate that the ATG8–ABS3 interaction represents a previously unknown non-autophagic function of ATG8.

ATG8–ABS3 interaction is required for ABS3-mediated senescence. Next, we sought to explore the functional consequence of disruption of the ATG8–ABS3 interaction. ATG8 is known to interact with its interactors via the ATG8-interacting motif (AIM)/LC3-interacting region (LIR)[47]. The iLIR programme predicts two potential AIMs in ABS3 and these two AIMs appear to be conserved in the ABS3 subfamily (Fig. 5a and Supplementary Fig. 6a)[48]. We constructed mutant forms of ABS3 harbouring mutations disrupting AIM1 (ABS3^{mAIM1}: W278A L281A) and AIM2 (ABS3^{mAIM2}: W463A L466A), individually and simultaneously (ABS3$^{mAIM1+mAIM2}$). Co-localization analyses indicated that three mutant forms of ABS3 did not affect late endosomal localization (Supplementary Fig. 6b). When individual AIM was disrupted, YN-ABS3^{mAIM1} or YN-ABS3^{mAIM2} could still reconstitute YFP with YC-ATG8e (Fig. 5b and Supplementary Fig. 6c). However, quantifications of BiFC assays showed that disruption of a single AIM, especially AIM2, significantly reduced the efficiency of the ATG8e–ABS3 interaction (Fig. 5b and Supplementary Fig. 5f). When both AIMs were mutated in ABS3$^{mAIM1+mAIM2}$, we observed a dramatically diminished interaction signal between YN-ABS3$^{mAIM1+mAIM2}$ and YC-ATG8e (Fig. 5b and Supplementary Fig. 5f), suggesting that these two AIMs are critical mediators of the ATG8–ABS3 interaction.

To investigate the cellular function of the ATG8–ABS3 interaction, we examined the trafficking of ABS3-GFP and ABS3$^{mAIM1+mAIM2}$-GFP in protoplasts. WT protoplasts transfected with *ABS3-GFP* were treated with the vacuolar protease inhibitor E-64d or mock-treated with dimethyl sulfoxide (DMSO) and incubated in sugar-free buffer in the dark for 12 h. In E-64d- but not DMSO-treated protoplasts, in addition to the endosomal ABS3-GFP

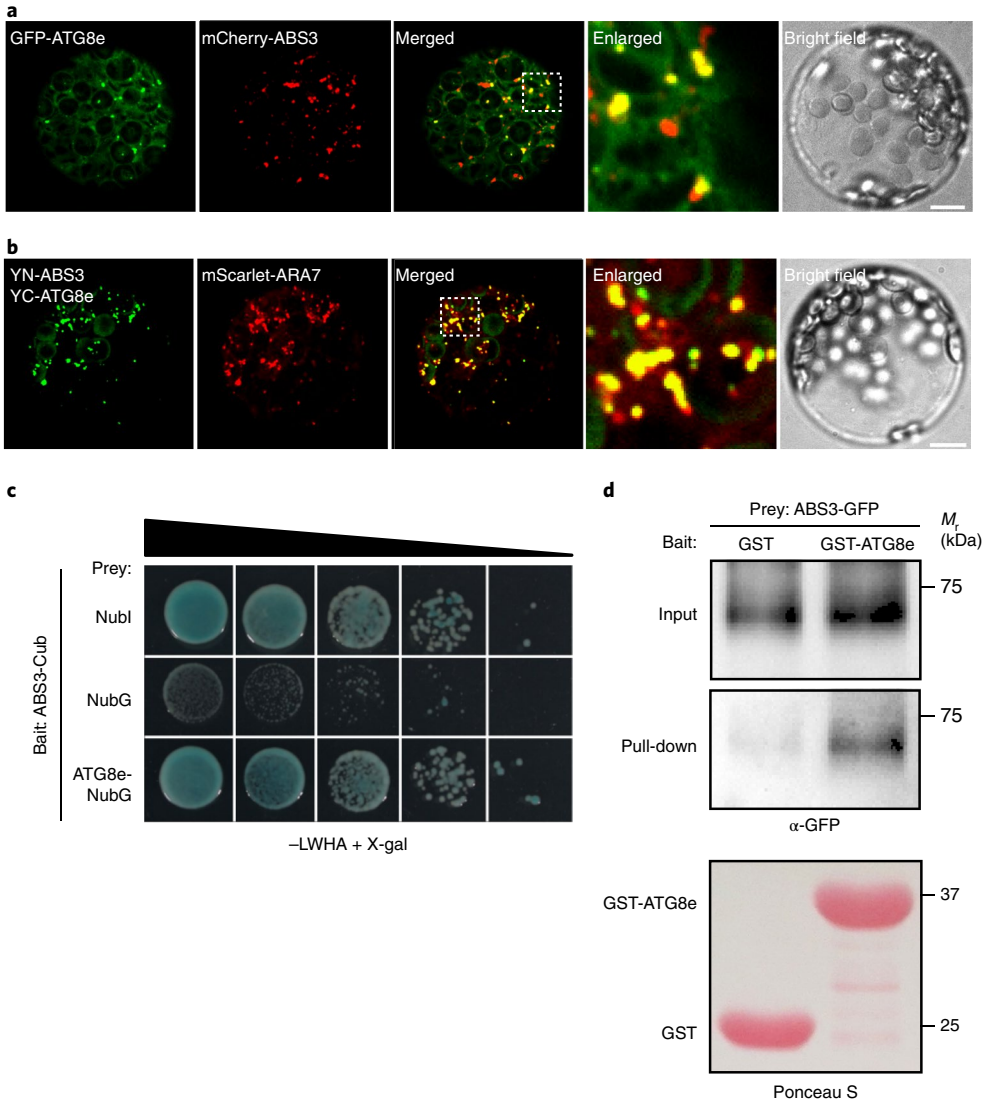

Fig. 3 | Physical interaction between ABS3 and ATG8e. a, Partial co-localization of GFP-ATG8e and mCherry-ABS3 in *Arabidopsis* leaf protoplasts. Scale bar, 10 μm. **b**, Protoplasts co-expressing YN-ABS3, YC-ATG8e and mScarlet-ARA7. Scale bar, 10 μm. **c**, Interaction between ABS3 and ATG8e in a split-ubiquitin assay. Cub, C-terminal half of ubiquitin; NubI, N-terminal half of native ubiquitin (positive control); NubG, N-terminal half of ubiquitin harbouring the I13G mutation (negative control). The growth of yeast colonies on quadruple dropout medium SD/–Leu/–Trp/–His/–Ade supplemented with X-gal (–LWHA + X-gal) is shown. **d**, GST pull-down assay with membrane fractions from *p35S:ABS3-GFP* transgenic lines. The experiments in **a**–**d** were repeated independently three times with similar results.

puncta present in the cell periphery, we also detected punctuate ABS3-GFP signals in the vacuole (Fig. 5c). The trafficking of ABS3-GFP to the vacuole was also observed in *atg7-3* or *atg5-1* backgrounds (Fig. 5c and Supplementary Fig. 6d). These findings suggest that under carbon deprivation ABS3-GFP is probably delivered to the vacuole for degradation, and this process is independent of autophagy. Strikingly, the delivery of ABS3-GFP to the vacuole was abolished when both AIMs were mutated, as $ABS3^{mAIM1+mAIM2}$-GFP maintained a predominantly endosomal distribution in either the WT or the *atg7-3*/*atg5-1* mutant background, regardless of the presence or absence of E-64d (Fig. 5c and Supplementary Fig. 6d). These data indicate that the trafficking of ABS3-GFP to the vacuole is dependent on the ATG8–ABS3 interaction but not autophagy.

To determine the trafficking of ABS3-GFP in planta, we tracked changes of ABS3-GFP and $ABS3^{mAIM1+mAIM2}$-GFP signals in *Arabidopsis* transgenic lines. In root epidermal cells of seedlings kept under light, both ABS3-GFP and $ABS3^{mAIM1+mAIM2}$-GFP showed endosomal localization, regardless of whether E-64d was added (Fig. 5d). In addition to the endosomal ABS3-GFP signals, 12 h of carbon deprivation led to diffused GFP signals in the vacuole (Fig. 5d). The addition of E-64d during carbon deprivation treatment led to the accumulation of ABS3-GFP puncta in the vacuole, confirming that the delivery of ABS3-GFP to the vacuole probably leads to its degradation. Consistently, immunoblotting analysis of ABS3-GFP showed a substantial increase of free GFP after carbon deprivation, and E-64d treatment during carbon deprivation increased the accumulation of ABS3-GFP with a concomitant decrease of free GFP (Supplementary Fig. 6e). Notably, this carbon-deprivation-stimulated trafficking of ABS3-GFP to the vacuole is disabled when AIMs in ABS3 are disrupted, as $ABS3^{mAIM1+mAIM2}$-GFP remained mostly endosomal even under carbon deprivation and E-64d treatment (Fig. 5d). Together, these data confirm that the ATG8–ABS3 interaction is required for the carbon-deprivation-induced vacuolar degradation of ABS3-GFP.

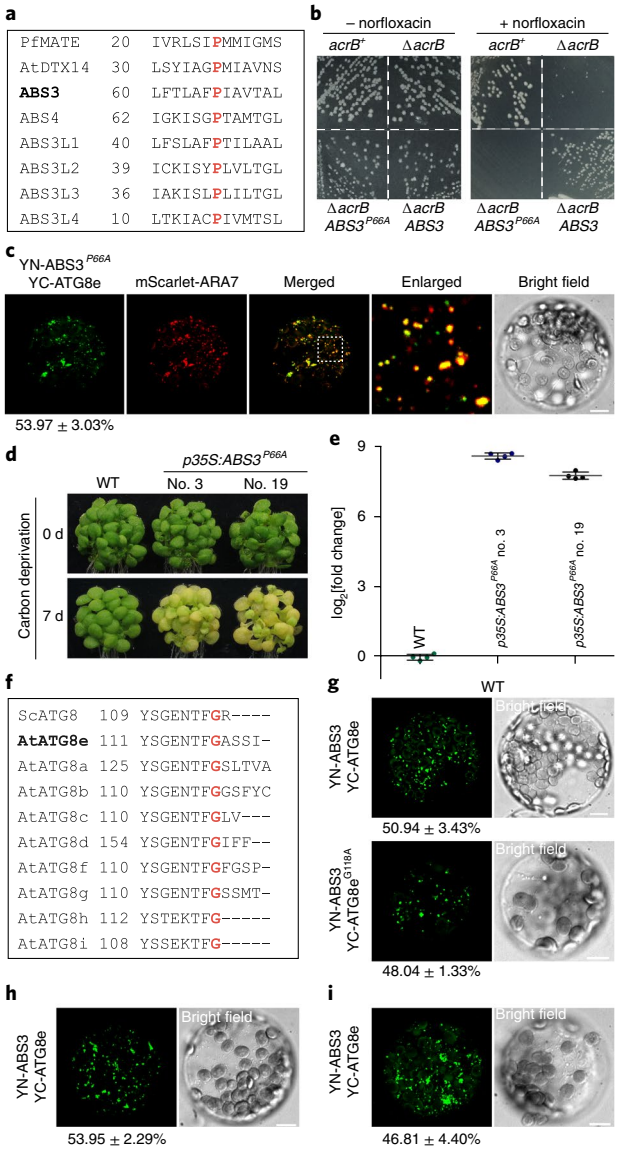

Fig. 4 | The ATG8–ABS3 interaction is independent of ABS3 transporter activity or ATG8-PE conjugation. a, Conserved proline residue in PfMATE, AtDTX14 and ABS3 subfamily MATEs. **b**, Growth complementation assays of the *E. coli ΔacrB* mutant expressing *ABS3* or *ABS3*^{P66A} on medium supplemented with antibiotic norfloxacin. **c**, Protoplasts co-expressing YN-ABS3^{P66A}, YC-ATG8e and mScarlet-ARA7. Scale bar, 10 μm. **d**, Senescence phenotypes of the WT and two independent lines expressing *p35S:ABS3*^{P66A} before and after 7 d of carbon deprivation. The experiments in **b** and **d** were repeated independently three times with similar results. **e**, RT-qPCR analysis of *ABS3* transcript levels in plants of the indicated genotypes. The log$_2$[fold change] was calculated with respect to the expression levels in the WT. Data are presented as means ± s.d. ($n = 4$ biological replicates). **f**, Conserved glycine residue in yeast (*Saccharomyces cerevisiae*) and *Arabidopsis* ATG8s. **g**, BiFC assays comparing the interaction between YN-ABS3 and YC-ATG8e and the interaction between YN-ABS3 and YC-ATG8e^{G118A} in WT leaf protoplasts. **h**,**i**, BiFC assays detecting the interaction between YN-ABS3 and YC-ATG8e in *atg5-1* (**h**) and *atg7-3* (**i**) protoplasts. Scale bars, 10 μm. Quantifications of BiFC assays in **c** and **g**–**i** were carried out by co-transfecting protoplasts with BiFC vectors and *p35S:mScarlet-ARA7* as the transfection control. The percentages of cells showing YFP signals over the total number of cells expressing mScarlet-ARA7 were calculated and are shown below each panel. Data are presented as means ± s.d. of three sets of experiments. See Supplementary Fig. 5 for the mScarlet-ARA7 panels of the same cells shown in **g**–**i** and the statistical analysis.

Finally, to uncover the physiological role of the ATG8–ABS3 interaction in planta, we generated *Arabidopsis* transgenic lines expressing *p35S:ABS3*$^{mAIM1+mAIM2}$. Despite the high levels of *ABS3*$^{mAIM1+mAIM2}$ transcripts, the progression of carbon-deprivation-induced senescence in *p35S:ABS3*$^{mAIM1+mAIM2}$ lines is comparable to that of the WT, in contrast with the accelerated senescence of *abs3-1D* (Fig. 5e and Supplementary Fig. 6f). Consistent with plant phenotypes, overexpression of *ABS3*$^{mAIM1+mAIM2}$ failed to accelerate protein degradation during carbon deprivation (Fig. 5f). When grown on soil, *p35S:ABS3*$^{mAIM1+mAIM2}$ lines resembled the WT but not *abs3-1D* (Supplementary Fig. 6g). To investigate whether the availability of the total cellular ATG8 pool regulates ABS3-mediated senescence, we overexpressed *ATG8e* in the *abs3-1D* background. Interestingly, the dramatically increased protein level of ATG8 did not alter the accelerated senescence of *abs3-1D* under carbon deprivation, nor did it affect the developmental phenotype of soil-grown *abs3-1D* (Fig. 5g,h and Supplementary Fig. 6h), suggesting that the amount of ATG8 is not a limiting factor of ABS3-mediated senescence. Together, these findings suggest that the ATG8–ABS3 interaction may generate a signal to promote senescence and protein degradation, and the involvement of ATG8 in the ABS3-mediated senescence pathway provides a function that is opposite to the role of autophagy in senescence prevention.

Conservation of the ATG8–ABS3 interaction in plant senescence. *ATG8* and MATE genes are ubiquitously present in higher plants. To test whether the ATG8–ABS3 interaction in dicotyledonous *Arabidopsis* represents a conserved mechanism in higher plants, we cloned an ABS3 subfamily MATE gene and an *ATG8* gene from monocotyledonous wheat (*Triticum aestivum*) and named these two genes *TaABS3* and *TaATG8d*, respectively, based on their phylogenetic relationship with *Arabidopsis* MATEs and ATG8s (Supplementary Figs. 1e and 7a,b). Co-localization of TaABS3-GFP with mScarlet-ARA7 in *Arabidopsis* protoplasts indicated that TaABS3 also resides at the late endosome (Fig. 6a). A BiFC assay showed that TaABS3 could interact with TaATG8d (Fig. 6b and Supplementary Fig. 7c). Moreover, we observed cross-species interactions between *Arabidopsis* ABS3 subfamily MATEs and TaATG8d (Supplementary Fig. 7d). Intriguingly, TaABS3 also harbours two putative AIMs at the conserved positions compared with those found in ABS3 (Fig. 6c). Consistent with findings in *Arabidopsis*, the disruption of both AIMs (mAIM1: W303A L306A; mAIM2: W488A L491A) in TaABS3 abolished the TaATG8d–TaABS3 interaction but did not interfere with the late endosomal localization of TaABS3 (Fig. 6d,e and Supplementary Fig. 7e). Lastly, we generated *Arabidopsis* transgenic lines expressing *p35S:TaABS3* or *p35S:TaABS3*$^{mAIM1+mAIM2}$. On carbon deprivation, *p35S:TaABS3* lines, but not *p35S:TaABS3*$^{mAIM1+mAIM2}$ lines, showed accelerated senescence and excessive loss of total cellular proteins compared with the WT (Fig. 6f–h). These data and the high homology between TaATG8d and AtATG8s suggest that the ABS3-mediated senescence pathway is probably conserved among dicot and monocot plants, and the ATG8–ABS3 interaction module represents a conserved senescence regulation paradigm in higher plants.

Discussion

Cellular proteostasis is a key determinant of senescence and longevity, and proteostasis dysfunction is often associated with premature senescence and diseases[1]. Protein degradation systems, including the canonical autophagy pathway, are expected to maintain cellular proteostasis[1]. In higher plants, defects in canonical autophagy lead to accelerated senescence under natural or stress conditions[35–38]. The counterintuitive fact that cellular protein degradation is accelerated in plant *atg* mutants suggests the presence of additional senescence pathway(s). However, the nature of these pathway(s) remains poorly understood.

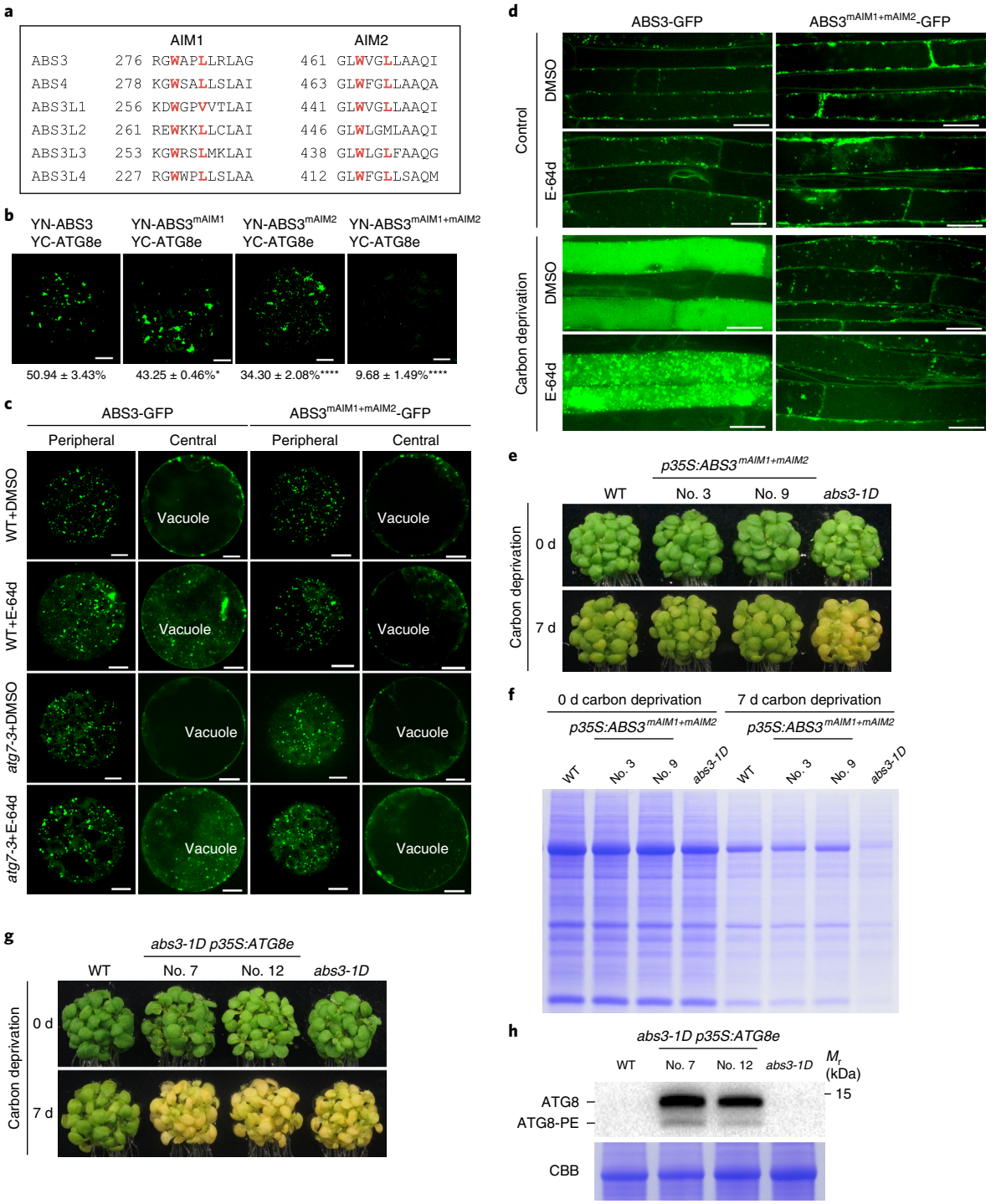

Fig. 5 | ABS3-mediated senescence requires ATG8–ABS3 interaction. a, Two conserved AIMs in ABS3 subfamily MATEs. **b**, BiFC assays to assess the interaction of YN-ABS3, YN-ABS3^{mAIM1}, YN-ABS3^{mAIM2} or YN-ABS3$^{mAIM1+mAIM2}$ with YC-ATG8e in *Arabidopsis* leaf protoplasts. Scale bars, 10 μm. Quantifications of BiFC assays are shown as means ± s.d. of three independent sets of experiments. *P = 0.0125 and ****P = 0.0001, one-way analysis of variance followed by Dunnett's multiple comparisons test. **c**, Subcellular distribution of transiently expressed ABS3-GFP and ABS3$^{mAIM1+mAIM2}$-GFP in the WT and *atg7-3* protoplasts treated with DMSO or E-64d. Images show the same protoplast focused to the periphery or to the centre of the cell. Scale bars, 10 μm. **d**, Root epidermal cells of *Arabidopsis* transgenic lines expressing ABS3-GFP or ABS3$^{mAIM1+mAIM2}$-GFP. Carbon deprivation treatment was carried out by transferring 4-day-old seedlings to liquid medium without sucrose and placing them in the dark for 12 h. Control plants were transferred to liquid medium with 1% sucrose and kept under light. The distribution patterns of ABS3-GFP or ABS3$^{mAIM1+mAIM2}$-GFP signals in the presence or absence of E-64d were examined. Scale bars, 20 μm. **e**, Senescence phenotype of the WT, two independent lines expressing *p35S:ABS3*$^{mAIM1+mAIM2}$, and *abs3-1D* before and after 7 d of carbon deprivation. **f**, Total cellular proteins from plants of the indicated genotypes before and after 7 d of carbon deprivation were resolved on SDS-PAGE and stained with CBB. **g**, Senescence phenotypes of the WT, two independent lines expressing *p35S:ATG8e* in *abs3-1D* background, and *abs3-1D* before and after 7 d of carbon deprivation. **h**, Immunoblot analysis of ATG8 and ATG8-PE accumulation in plants of the indicated genotypes. Total leaf proteins from three-week-old plants were analysed. The experiments in **c**–**h** were repeated independently three times with similar results.

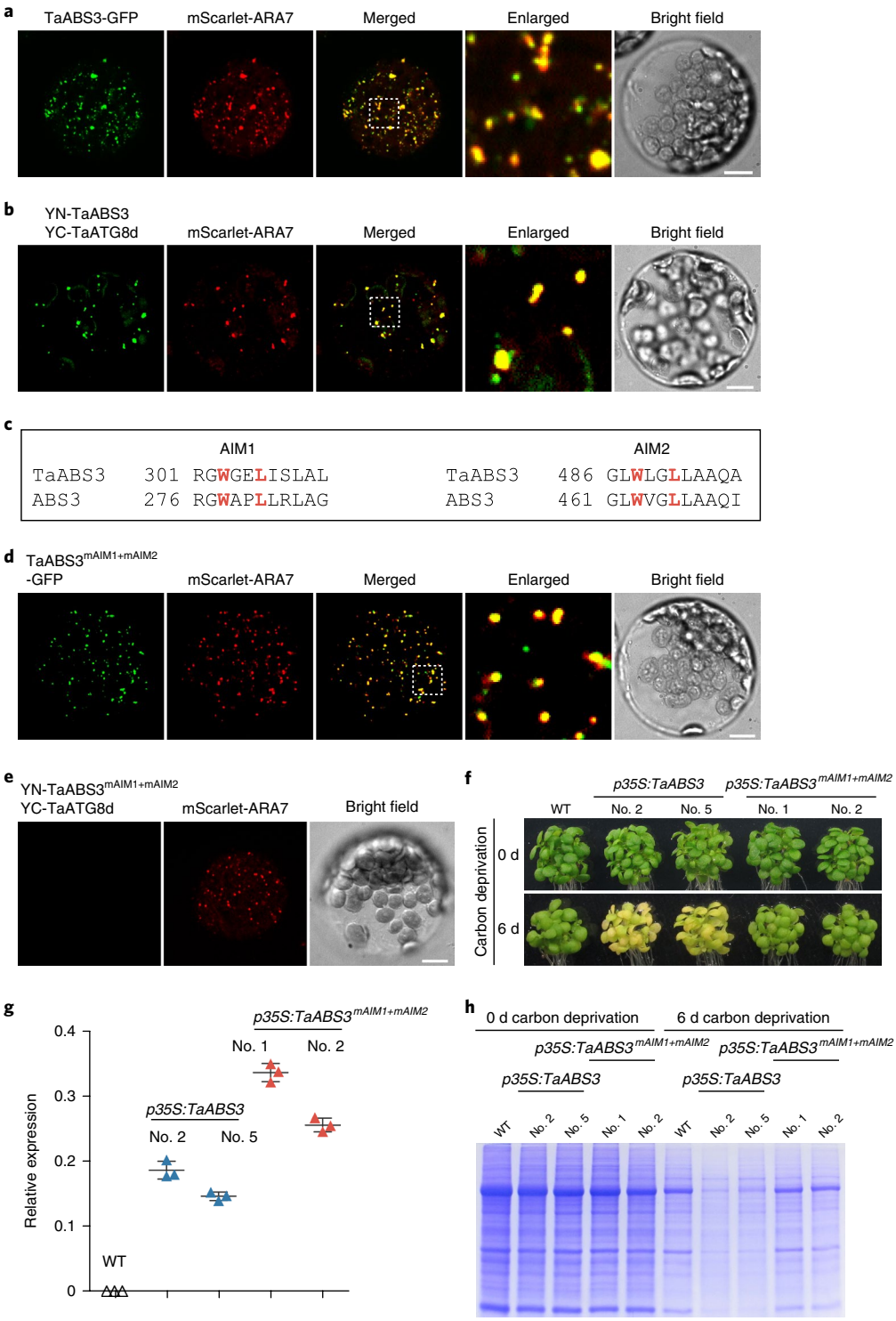

Fig. 6 | Conserved ATG8–ABS3 interactions in wheat. a, Co-localization of TaABS3-GFP and mScarlet-ARA7 in *Arabidopsis* leaf protoplasts. **b**, Protoplasts co-expressing YN-TaABS3, YC-TaATG8d and mScarlet-ARA7. **c**, Two conserved AIMs in TaABS3. **d**, Co-localization of TaABS3$^{mAIM1+mAIM2}$-GFP and mScarlet-ARA7 in *Arabidopsis* protoplasts. **e**, Protoplasts co-expressing YN-TaABS3$^{mAIM1+mAIM2}$, YC-TaTAG8d and mScarlet-ARA7. Scale bars in **a**,**b**,**d** and **e**, 10 μm. **f**, Senescence phenotypes of the WT, two independent lines expressing *p35S:TaABS3*, and two independent lines expressing *p35S:TaABS3*$^{mAIM1+mAIM2}$ before and after 6 d of carbon deprivation. **g**, RT-qPCR analysis of *TaABS3* transcript levels in plants of the indicated genotypes. Relative expressions of *TaABS3* were normalized to *ACT2*. Data are presented as means ± s.d. ($n = 3$ biological replicates). **h**, Total cellular proteins from plants of the indicated genotypes before and after 6 d of carbon deprivation were resolved on SDS-PAGE and stained with CBB. The experiments in **a**,**b**,**d**–**f** and **h** were repeated independently three times with similar results.

In this study, we discovered that six late endosome-localized *Arabidopsis* ABS3 subfamily MATE transporters act redundantly to promote natural and carbon-deprivation-induced senescence (Figs. 1 and 5). The hypersensitivity to carbon deprivation of *ABS3* gain-of-function mutants is reminiscent of loss-of-function mutants in autophagy[2,3], suggesting opposite consequences of the

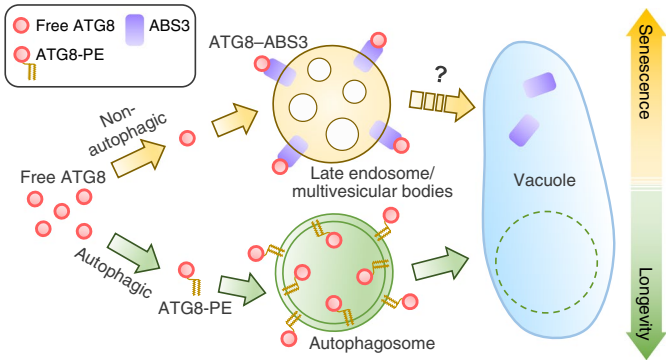

Fig. 7 | Model for the ATG8–ABS3 interaction in controlling senescence in plants. See 'Discussion' for a detailed explanation of the model.

two catabolic pathways. However, clear functional distinctions exist between the ABS3-mediated pathway and autophagy, as *ABS3* gain-of-function mutants display additional developmental phenotypes that are not associated with plant autophagy mutants[27,30]. In-depth genetic dissection of the ABS3-mediated pathway and autophagy pathway showed that the accelerated protein degradation and senescence phenotypes of *atg* mutants were suppressed by the higher-order MATE gene family mutants but further worsened in *abs3-1D* (Fig. 2). The *mateq* mutant could circumvent autophagy deficiency to prevent senescence and promote plant longevity during carbon deprivation. Our findings suggest that ABS3 subfamily MATE transporters are required for the senescence programme under carbon deprivation or canonical autophagy deficiency.

Furthermore, we discovered that ABS3 subfamily MATEs interact with ATG8 at the late endosome to promote senescence (Fig. 3). The C-terminal processing of ATG8, subsequent conjugation of ATG8 to ATG8-PE and recruitment of ATG8-PE to autophagic membranes are conserved and obligatory steps in autophagy[3,15]. In contrast, the ATG8–ABS3 interaction at the late endosome does not require the formation of ATG8-PE or ATG5/7-dependent canonical autophagy (Figs. 4f–i and 5e). Thus, our findings reveal a non-autophagic function of ATG8 in the ABS3-mediated senescence pathway. Importantly, this ABS3-mediated pathway is probably conserved in higher plants as we observed a similar TaATG8–TaABS3 function module in monocotyledonous wheat (Fig. 6). Although non-autophagic functions of ATG proteins have recently emerged[49,50], the discovery that the ATG8–ABS3 interaction controls plant senescence is unprecedented. Given the membrane tethering ability of ATG8 and the potential large number of ATG8-interacting proteins in plants and animals[51,52], ATG8 and related proteins could act as central and versatile facilitators of cellular processes beyond autophagy. The identification of ABS3 subfamily MATEs as novel ATG8 interactors expands the known ATG8 interactome and cellular functions.

Based on our findings, we propose a model in which the ATG8–ABS3 pathway and canonical autophagy act in parallel and control plant senescence and longevity (Fig. 7). Under mild nutrient limitation, autophagy is activated and utilizes ATG8 to promote plant longevity. However, under severe nutrient deprivation, or when autophagy is blocked, the previously unrecognized ATG8–ABS3 pathway promotes plant senescence (Fig. 7). Under carbon deprivation, the ATG8–ABS3 interaction promotes ABS3 trafficking to the vacuole lumen and its degradation in the vacuole (Fig. 5). The trafficking of ABS3 into the vacuole is clearly independent of autophagy. Given the presence of ABS3 on the late endosome, ABS3-GFP trafficking may be mediated by endosomal vacuole fusion. However, how ABS3-GFP is delivered to the vacuole lumen remains unclear, and additional mechanisms might be involved[53]. Since ABS3-mediated senescence is neither alleviated nor enhanced by the increased amount of ATG8 protein (Fig. 5g), additional factors may be needed for the partitioning of ATG8s to the senescence-preventing autophagy pathway or the senescence-promoting ABS3 pathway. It is possible that the interaction between the ATG8–ABS3 interaction and the subsequent degradation of ABS3 in the vacuole triggers a retrograde signal that activates the senescence programme in a nutrient-dependent manner. In this scenario, the flux of ABS3 to the vacuole may serve as a means for the vacuole to sense the nutrient status of the cell. Our findings uncover a new non-autophagic function of ATG8 and establish the noncanonical ATG8–ABS3 pathway as an evolutionarily conserved senescence regulatory mechanism in higher plants.

Methods

Plant materials and growth conditions. All *Arabidopsis* strains used in this study are of the Columbia-0 (Col-0) background. *Arabidopsis* mutants *atg5-1* (SAIL_129_B07)[37], *atg7-3* (SAIL_11_H07)[54], *abs3-1D*[30], *abs4-1D*[30], *abs3-1* (SM3_36823)[30], *abs4-1* (SALK_067667)[30], *abs3l1-1* (SAIL_1236_H10)[30] and *abs3l2-1* (SALK_144096)[30] have been described; *abs3l3-1* (SALK_127812) and *abs3l4-1* (SALK_128217) were obtained from the *Arabidopsis* Biological Resource Center. The quadruple mutant *mateq* (*abs3-1 abs4-1 abs3l1-1 abs3l2-1*) has been described[30]. The higher-order mutants *mated* (the *abs3-1 abs4-1* double mutant), *mates* (the *abs3-1 abs4-1 abs3l1-1 abs3l2-1 abs3l3-1 abs3l4-1* sextuple mutant), the *abs3-1D atg7-3* double mutant, the *mateq atg7-3* quintuple mutant, the *abs3-1D atg5-1* double mutant and the *mateq atg5-1* quintuple mutant were generated in this study. The *Arabidopsis* transgenic line expressing *pUBQ10:YFP-ARA7* (wave_2Y) has been described[55]. The primers used for genotyping are listed in Supplementary Table 1.

Plants for protoplast preparation were grown on Jiffy-7-Peat Pellets (Jiffy Group) and kept in a growth chamber set at 22 °C and under ~75 μmol m^{-2} s^{-1} illumination in a 12 h/12 h day/night cycle. Plants for other purposes were grown on commercial soil mix (Pindstrup) and placed in a growth room kept at 22 °C with continuous illumination at ~80 μmol m^{-2} s^{-1}.

Carbon deprivation treatment. *Arabidopsis* seeds were first surface sterilized with a solution containing 50% (*v/v*) bleach and 0.1% (*v/v*) Triton X-100 for 5 min and washed 7 times with sterilized water. After 3 d of stratification at 4 °C, the seeds were planted on a 1/2 Murashige and Skoog basal salts mixture (M153; PhytoTechnology Laboratories) supplemented with 1% (*w/v*) sucrose and 1% (*w/v*) Bacto Agar (214010, BD). 1/2 Murashige and Skoog plates were then placed vertically in a growth chamber under continuous illumination at ~75 μmol m^{-2} s^{-1}. For the carbon deprivation treatment, 7-day-old seedlings were transferred to 1/2 Murashige and Skoog plates without sucrose and wrapped in aluminium foil for dark treatment in the same growth chamber for the indicated time periods. Seedlings immediately after transplantation served as 0 d carbon deprivation controls.

Nitrogen starvation treatment. *Arabidopsis* seeds were sown on a 1/2 Murashige and Skoog basal salts mixture without nitrogen (M531; PhytoTechnology Laboratories) supplemented with 10 mM KNO_3, 1% (*w/v*) sucrose and 1% (*w/v*) Bacto Agar. Seven-day-old seedlings were then transferred to the same medium with 10 mM KCl (nitrogen starvation) or 10 mM KNO_3 (control treatment) for 4 d. Plants were kept under continuous light (~80 μmol m^{-2} s^{-1}) at 22 °C before and during nitrogen starvation.

Vector construction. Details of the primers used for vector construction are listed in Supplementary Table 1. A list of all of the vectors used in this study is provided in Supplementary Table 2.

Briefly, for co-localization studies, coding sequences of the fluorescent proteins GFP, mCherry and mScarlet[42] with or without the stop codon were amplified and placed in the *pUC18* backbone between the 35S promoter and NOS terminator. Coding sequences of *Arabidopsis* MATE family genes were fused at the N terminus of GFP coding sequences to generate *pUC18-p35S:MATE-GFP*. Coding sequences of *Arabidopsis ATG8* genes were fused at the C terminus of GFP to generate *pUC18-p35S:GFP-ATG8*. *TaABS3* and *TaATG8d* messenger RNA sequences were obtained by performing blast searches using ABS3 and ATG8e protein sequences as queries, respectively. *TaABS3* and *TaATG8d* complementary DNA (cDNA) sequences were amplified from cDNAs synthesized from wheat seedlings, cloned into the *pUC18-p35S:GFP* vector and verified by sequencing. Coding sequences of *ARA7* were fused at the C terminus of mScarlet to generate *pUC18-p35S:mScarlet-ARA7*. Coding sequences of *ABS3* were fused at the C terminus of mCherry to generate *pUC18-p35S:mCherry-ABS3*. Vectors harbouring mutated versions of *ABS3*, *TaABS3* or *Arabidopsis ATG8e* were generated using the Q5 Site-Directed Mutagenesis Kit (E0554S; New England Biolabs). For the BiFC assay, the expression cassettes for YN and YC, together with the polylinker sequence, were digested from *pSPYNE(R)173* and *pSPYCE(M)*[43], and cloned into the pUC18

backbone to generate *pUC18-p35S:YN* and *pUC18-p35S:YC*, respectively. Coding sequences of MATE family genes were fused at the C terminus of YN to generate *pUC18-p35S:YN-MATE*. Coding sequences of nine *Arabidopsis ATG8* genes and wheat *TaATG8d* were fused at the C terminus of YC to generate *pUC18-p35S:YC-ATG8*. Vectors for the split-ubiquitin assay were constructed as described previously[44].

Generation of transgenic lines. For plant transformation, coding sequences for ABS3-GFP, ABS3^{P66A}, ABS3$^{mAIM1+mAIM2}$, ABS3$^{mAIM+mAIM2}$-GFP, TaABS3, TaABS3$^{mAIM+mAIM2}$ and ATG8e were subcloned into a binary vector *pBI111L*[56] between the 35S promoter and NOS terminator. *pBI111L-pABS3:ABS3-GFP* was generated by replacing the 35S promoter in *pBI111L* with *ABS3* endogenous promoter sequences[30]. The floral dip method was used for generating transgenic lines[57]. T1 plants were screened on solid 1/2 Murashige and Skoog medium supplemented with 1% (*w/v*) sucrose, 1% (*w/v*) Bacto Agar and 50 μg ml^{-1} kanamycin.

Protein and chlorophyll contents measurement. To measure protein and chlorophyll contents from the same sample, whole seedlings were harvested from vertical plates, weighed, frozen and ground in liquid nitrogen. Ground tissues were resuspended in 50 mM Tris-HCl pH 6.8, 2% sodium dodecyl sulfate (SDS) and 10% glycerol. A 50 μl tissue resuspension from each sample was saved for chlorophyll measurement. The rest of the tissue resuspensions were incubated at 95 °C for 5 min to extract protein. Supernatants were collected after spinning at 14,000 r.p.m. at room temperature for 10 min. Protein contents in supernatants were measured using a Pierce BCA Protein Assay Kit (23227; Thermo Fisher Scientific) following the manufacturer's instructions. Chlorophyll was extracted by adding 450 μl 95% ethanol to 50 μl tissue resuspension and incubating at 4 °C in the dark. Supernatants were separated from tissue debris by centrifugation at 14,000 r.p.m. at 4 °C for 10 min. Absorbances at 649 and 664 nm of the supernatant were measured. The chlorophyll content was calculated as described previously[58]. Protein and chlorophyll contents were normalized to equal amounts of fresh tissue weight. Three biological replicates were included.

Immunoblot analysis. For SDS polyacrylamide gel electrophoresis (SDS-PAGE) and immunoblotting, seedlings were weighed, frozen and ground in liquid nitrogen, and incubated with the lysis buffer containing 0.125 M Tris-HCl pH 6.8, 4% SDS and 20% glycerol for 2 h at 65 °C. Samples were normalized by adjusting the lysis buffer volumes based on the fresh tissue weight. After incubation, total cell extracts were centrifuged at 14,000 r.p.m. for 10 min at room temperature to remove the tissue debris.

To compare the total cellular protein levels in different samples and to separate ATG8 and ATG8-PE, a Urea-Tricine SDS-PAGE system was utilized[59]. Proteins were then transferred onto a polyvinylidene difluoride membrane and probed with a polyclonal ATG8 antibody prepared in-house. The ATG8 antibody was prepared as described previously[60]. To detect NBR1, RBCL and PBA1, protein samples were separated by standard SDS-PAGE, transferred onto a nitrocellulose membrane and probed with specific antibodies (anti-NBR1, AS142805 (Agrisera); anti-RBCL AS03037 (Agrisera); anti-PBA1, ab98861 (Abcam)).

RNA extraction and reverse-transcription quantitative PCR (RT-qPCR). Total RNAs were prepared from seedlings using the Trizol RNA reagent (15596018; Thermo Fisher Scientific) following the manufacturer's instructions. cDNA was synthesized from 1 μg total RNA using the Transcriptor First Strand cDNA Synthesis Kit (04897030001; Roche). qPCRs were performed using FastStart Essential DNA Green Master (06924204001; Roche) on a CFX96 Touch Real-Time PCR Detection System (Bio-Rad). The primers for qPCRs are listed in Supplementary Table 1. Three or four biological replicates were included for data quantification. The expression of *ACT2* was used as an internal control.

Split-ubiquitin assay. The procedure for the split-ubiquitin assay has been described previously[44]. Briefly, to detect an interaction between ATG8e and ABS3, *XN21 ATG8e-NubG* and *MetYC ABS3-CubPLV* were co-transformed into the yeast strain THY.AP4. To detect an interaction between ATG8e and ABS4, *NX33 NubG-ATG8e* and *MetYC ABS4-CubPLV* were co-transformed into the yeast strain THY.AP4. Different NubG vectors were used to minimize the false positive interaction. Co-transformed yeast cells were selected on SD-Leu-Trp medium. Single colonies were inoculated in liquid SD-Leu-Trp medium, and tenfold serial dilutions from saturated liquid cultures were spotted on SD-Leu-Trp-His-Ade + X-gal selection medium to detect protein interactions.

Protoplast transfection and spinning-disk confocal microscopy. *Arabidopsis* leaf protoplasts were prepared as described previously[61]. For co-transfections, 10 μg of each vector were used to transfect 200 μl protoplasts (2×10^5 ml^{-1}). After transfection, protoplasts were incubated for 10–12 h before being examined with a spinning-disk confocal system equipped with a CSU-W1 spinning-disk head (Yokogawa) and an iXon Ultra 888 EMCCD (Andor) on a DMi8 microscope body (Leica). Specifically, protoplasts were imaged with a HCX PL Apo 1.44 N.A. 100× oil immersion objective. GFP and YFP were excited at 488 nm. mCherry and mScarlet signals were excited at 561 nm. A TR-F525/50 or TR-F593/46 bandpass emission filter (Semrock BrightLine) was used for capturing GFP/YFP or mCherry/mScarlet signals. Confocal images were processed with the Fiji ImageJ software[62]. To quantify BiFC assays, *p35S:mScarlet-ARA7* was co-transfected with BiFC vectors as a transfection control. Interactions of YN and YC fusion proteins were quantified as the percentage of total transfected cells with YFP signals (cells with mScarlet-ARA7 signals). Three independent sets of experiments were performed and quantified for each pair of YN and YC vectors. Note that BiFC quantification data summarized in Supplementary Fig. 5f are also shown in Figs. 4c,g–i and 5b as means ± s.d.

Magic Red Cathepsin B assay. Magic Red Cathepsin B staining was performed on protoplasts prepared from cotyledons of 7-d-old seedlings following the manufacturer's instructions (number 937; ImmunoChemistry Technologies). After incubation, protoplasts were imaged using a fluorescence microscope (DMi8; Leica) equipped with a DFC365 FX CCD (Leica) using the 10× objective lens. The fluorescence intensities of each cell were measured using the Fiji ImageJ software.

GST pull-down assay. Recombinant GST or GST-ATG8e proteins were produced by transforming *E. coli* strain BL21(DE3) with *pGEX 4T-1* (27-4580-01; GE Healthcare) or *pGEX 4T-1-ATG8e* and purified with Glutathione Sepharose 4B beads (17-0756-01; GE Healthcare) following the manufacturer's instructions. To pull down ABS3-GFP from *p35S:ABS3-GFP* transgenic lines, the membrane fraction was prepared from 0.5 g fresh tissue of *p35S:ABS3-GFP* plants as described[63] and incubated with 10 μl Glutathione Sepharose 4B beads loaded with 100 μg of purified GST or GST-ATG8e at 4 °C overnight in pull-down buffer (100 mM Tris-HCl pH 7.3, 150 mM NaCl, 1 mM ethylenediaminetetraacetic acid, 1% Triton X-100, 10% Glycerol and 1× protease inhibitor cocktail (4693159001; Roche)). After incubation, the beads were washed 5 times with washing buffer (100 mM Tris-HCl pH 7.3, 150 mM NaCl, 1 mM ethylenediaminetetraacetic acid and 1× protease inhibitor cocktail (4693159001, Roche)) and eluted by boiling in 2× SDS sample buffer. The presence of ABS3-GFP in the elutes was detected by immunoblotting using a monoclonal anti-GFP antibody (632381; Clontech).

***E. coli* mutant growth complementation assay.** The growth complementation assay was carried out using the drug-sensitive *E. coli* strain (BW25113) *ΔacrB* as described previously[45]. In brief, coding sequences for ABS3 or ABS3^{P66A} were cloned into *pMAL-c4X* (New England Biolabs) and the resulting vectors *pMAL-c4X-ABS3* and *pMAL-c4X-ABS3^{P66A}* were used to transform the *ΔacrB* strain. Transformants were steaked on lysogeny broth plates containing 0.25 mM isopropyl β-D-1-thiogalactopyranoside to induce the expression of *ABS3* or *ABS3^{P66A}*. Norfloxacin (0.02 μg ml^{-1}) (70458967; Sigma) was added to the plates to test drug resistance.

Drug treatment. To treat protoplasts with E-64d (sc-201280A; Santa Cruz Biotechnology), 20 μM E-64d or an equal volume of DMSO (0.1% (*v/v*)) was added to the protoplast incubation solution immediately after transfection. To treat seedlings with E-64d, 7-day-old seedlings grown on vertical plates were transferred to liquid 1/2 Murashige and Skoog medium containing 20 μM E-64d or an equal volume of DMSO (0.1%(*v/v*)). To treat seedlings with wortmannin (S2758; Selleck), 4-day-old seedlings grown on vertical plates were transferred to liquid 1/2 Murashige and Skoog medium containing 30 μM wortmannin or an equal volume of DMSO (0.1% (*v/v*)) for 1 h before examination by spinning-disk confocal microscopy.

Accession numbers. Sequence data for the genes used in this study can be found in The *Arabidopsis* Information Resource (www.arabidopsis.org) under the following accession numbers: ABS3, At4g29140; ABS4, At1g58340; ABS3L1, At5g19700; ABS3L2, At5g52050; ABS3L3, At4g23030; ABS3L4, At2g38510; ATG8a, At4g21980; ATG8b, At4g04620; ATG8c, At1g62040; ATG8d, At2g05630; ATG8e, At2g45170; ATG8f, At4g16520; ATG8g, At3g60640; ATG8h, At3g06420; ATG8i, At3g15580; ARA7, At4g19640.

Reporting Summary. Further information on research design is available in the Nature Research Reporting Summary linked to this article.

Data availability

The data that support the findings of this study are available from the corresponding author upon reasonable request.

Received: 19 May 2018; Accepted: 13 December 2018;
Published online: 21 January 2019

References

1. Riera, C. E., Merkwirth, C., De Magalhaes Filho, C. D. & Dillin, A. Signaling networks determining life span. *Annu. Rev. Biochem.* **85**, 35–64 (2016).
2. Li, F. & Vierstra, R. D. Autophagy: a multifaceted intracellular system for bulk and selective recycling. *Trends Plant Sci.* **17**, 526–537 (2012).

3. Liu, Y. & Bassham, D. C. Autophagy: pathways for self-eating in plant cells. *Annu. Rev. Plant Biol.* **63**, 215–237 (2012).
4. Xiong, Y. et al. Glucose-TOR signalling reprograms the transcriptome and activates meristems. *Nature* **496**, 181–186 (2013).
5. Sheen, J. Master regulators in plant glucose signaling networks. *J. Plant Biol.* **57**, 67–79 (2014).
6. Xiong, Y. & Sheen, J. Novel links in the plant TOR kinase signaling network. *Curr. Opin. Plant Biol.* **28**, 83–91 (2015).
7. Baena-González, E., Rolland, F., Thevelein, J. M. & Sheen, J. A central integrator of transcription networks in plant stress and energy signalling. *Nature* **448**, 938–942 (2007).
8. Lim, P. O., Kim, H. J. & Nam, H. G. Leaf senescence. *Annu. Rev. Plant Biol.* **58**, 115–136 (2007).
9. Thomas, H. Senescence, ageing and death of the whole plant. *New Phytol.* **197**, 696–711 (2013).
10. Woo, H. R., Kim, H. J., Nam, H. G. & Lim, P. O. Plant leaf senescence and death—regulation by multiple layers of control and implications for aging in general. *J. Cell Sci.* **126**, 4823–4833 (2013).
11. Kim, J., Woo, H. R. & Nam, H. G. Toward systems understanding of leaf senescence: an integrated multi-omics perspective on leaf senescence research. *Mol. Plant* **9**, 813–825 (2016).
12. Guo, Y. & Gan, S.-S. Convergence and divergence in gene expression profiles induced by leaf senescence and 27 senescence-promoting hormonal, pathological and environmental stress treatments. *Plant Cell Environ.* **35**, 644–655 (2012).
13. Liebsch, D. & Keech, O. Dark-induced leaf senescence: new insights into a complex light-dependent regulatory pathway. *New Phytol.* **212**, 563–570 (2016).
14. Kaur, J. & Debnath, J. Autophagy at the crossroads of catabolism and anabolism. *Nat. Rev. Mol. Cell Biol.* **16**, 461–472 (2015).
15. Xie, Z. & Klionsky, D. J. Autophagosome formation: core machinery and adaptations. *Nat. Cell Biol.* **9**, 1102–1109 (2007).
16. Michaeli, S., Galili, G., Genschik, P., Fernie, A. R. & Avin-Wittenberg, T. Autophagy in plants—what's new on the menu?. *Trends Plant Sci.* **21**, 134–144 (2016).
17. Soto-Burgos, J., Zhuang, X., Jiang, L. & Bassham, D. C. Dynamics of autophagosome formation. *Plant Physiol.* **176**, 219–229 (2018).
18. Morita, Y., Kataoka, A., Shiota, S., Mizushima, T. & Tsuchiya, T. NorM of *Vibrio parahaemolyticus* is an Na^+-driven multidrug efflux pump. *J. Bacteriol.* **182**, 6694–6697 (2000).
19. Ogawa, T. et al. Stimulating S-adenosyl-L-methionine synthesis extends lifespan via activation of AMPK. *Proc. Natl Acad. Sci. USA* **113**, 11913–11918 (2016).
20. Otsuka, M. et al. A human transporter protein that mediates the final excretion step for toxic organic cations. *Proc. Natl Acad. Sci. USA* **102**, 17923–17928 (2005).
21. Li, L., He, Z., Pandey, G. K., Tsuchiya, T. & Luan, S. Functional cloning and characterization of a plant efflux carrier for multidrug and heavy metal detoxification. *J. Biol. Chem.* **277**, 5360–5368 (2002).
22. Diener, A. C., Gaxiola, R. A. & Fink, G. R. *Arabidopsis* ALF5, a multidrug efflux transporter gene family member, confers resistance to toxins. *Plant Cell* **13**, 1625–1638 (2001).
23. Rogers, E. E. & Guerinot, M. L. FRD3, a member of the multidrug and toxin efflux family, controls iron deficiency responses in *Arabidopsis*. *Plant Cell* **14**, 1787–1799 (2002).
24. Magalhaes, J. V. et al. A gene in the multidrug and toxic compound extrusion (MATE) family confers aluminum tolerance in sorghum. *Nat. Genet.* **39**, 1156–1161 (2007).
25. Marinova, K. et al. The *Arabidopsis* MATE transporter TT12 acts as a vacuolar flavonoid/H^+-antiporter active in proanthocyanidin-accumulating cells of the seed coat. *Plant Cell* **19**, 2023–2038 (2007).
26. Serrano, M. et al. Export of salicylic acid from the chloroplast requires the multidrug and toxin extrusion-like transporter EDS5. *Plant Physiol.* **162**, 1815–1821 (2013).
27. Li, R. et al. ADP1 affects plant architecture by regulating local auxin biosynthesis. *PLoS Genet.* **10**, e1003954 (2014).
28. Zhang, H. et al. A DTX/MATE-type transporter facilitates abscisic acid efflux and modulates ABA sensitivity and drought tolerance in *Arabidopsis*. *Mol. Plant* **7**, 1522–1532 (2014).
29. Tian, W. et al. A molecular pathway for CO_2 response in *Arabidopsis* guard cells. *Nat. Commun.* **6**, 6057 (2015).
30. Wang, R. et al. A subgroup of MATE transporter genes regulates hypocotyl cell elongation in *Arabidopsis*. *J. Exp. Bot.* **66**, 6327–6343 (2015).
31. Zhang, H. et al. Two tonoplast mate proteins function as turgor-regulating chloride channels in *Arabidopsis*. *Proc. Natl Acad. Sci. USA* **114**, E2036–E2045 (2017).
32. Dobritzsch, M. et al. MATE transporter-dependent export of hydroxycinnamic acid amides. *Plant Cell* **28**, 583–596 (2016).
33. Kim, J. H. et al. Trifurcate feed-forward regulation of age-dependent cell death involving miR164 in *Arabidopsis*. *Science* **323**, 1053–1057 (2009).
34. Sato, Y., Morita, R., Nishimura, M., Yamaguchi, H. & Kusaba, M. Mendel's green cotyledon gene encodes a positive regulator of the chlorophyll-degrading pathway. *Proc. Natl Acad. Sci. USA* **104**, 14169–14174 (2007).
35. Hanaoka, H. et al. Leaf senescence and starvation-induced chlorosis are accelerated by the disruption of an *Arabidopsis* autophagy gene. *Plant Physiol.* **129**, 1181–1193 (2002).
36. Doelling, J. H., Walker, J. M., Friedman, E. M., Thompson, A. R. & Vierstra, R. D. The APG8/12-activating enzyme APG7 is required for proper nutrient recycling and senescence in *Arabidopsis thaliana*. *J. Biol. Chem.* **277**, 33105–33114 (2002).
37. Thompson, A. R., Doelling, J. H., Suttangkakul, A. & Vierstra, R. D. Autophagic nutrient recycling in *Arabidopsis* directed by the ATG8 and ATG12 conjugation pathways. *Plant Physiol.* **138**, 2097–2110 (2005).
38. Phillips, A. R., Suttangkakul, A. & Vierstra, R. D. The ATG12-conjugating enzyme ATG10 is essential for autophagic vesicle formation in *Arabidopsis thaliana*. *Genetics* **178**, 1339–1353 (2008).
39. Svenning, S., Lamark, T., Krause, K. & Johansen, T. Plant NBR1 is a selective autophagy substrate and a functional hybrid of the mammalian autophagic adapters NBR1 and p62/SQSTM1. *Autophagy* **7**, 993–1010 (2011).
40. Cui, Y. et al. Biogenesis of plant prevacuolar multivesicular bodies. *Mol. Plant* **9**, 774–786 (2016).
41. Lee, G.-J., Sohn, E. J., Lee, M. H. & Hwang, I. The *Arabidopsis* rab5 homologs rha1 and ara7 localize to the prevacuolar compartment. *Plant Cell Physiol.* **45**, 1211–1220 (2004).
42. Bindels, D. S. et al. mScarlet: a bright monomeric red fluorescent protein for cellular imaging. *Nat. Methods* **14**, 53–56 (2017).
43. Waadt, R. et al. Multicolor bimolecular fluorescence complementation reveals simultaneous formation of alternative CBL/CIPK complexes in planta. *Plant J.* **56**, 505–516 (2008).
44. Bashline, L. & Gu, Y. Using the split-ubiquitin yeast two-hybrid system to test protein–protein interactions of transmembrane proteins. *Methods Mol. Biol.* **1242**, 143–158 (2015).
45. Tanaka, Y. et al. Structural basis for the drug extrusion mechanism by a MATE multidrug transporter. *Nature* **496**, 247–251 (2013).
46. Miyauchi, H. et al. Structural basis for xenobiotic extrusion by eukaryotic MATE transporter. *Nat. Commun.* **8**, 1633 (2017).
47. Birgisdottir, Å. B., Lamark, T. & Johansen, T. The LIR motif—crucial for selective autophagy. *J. Cell Sci.* **126**, 3237–3247 (2013).
48. Jacomin, A.-C., Samavedam, S., Charles, H. & Nezis, I. P. iLIR@viral: a web resource for LIR motif-containing proteins in viruses. *Autophagy* **13**, 1782–1789 (2017).
49. Subramani, S. & Malhotra, V. Non-autophagic roles of autophagy-related proteins. *EMBO Rep.* **14**, 143–151 (2013).
50. Schaaf, M. B. E., Keulers, T. G., Vooijs, M. A. & Rouschop, K. M. A. LC3/GABARAP family proteins: autophagy-(un)related functions. *FASEB J.* **30**, 3961–3978 (2016).
51. Kriegenburg, F., Ungermann, C. & Reggiori, F. Coordination of autophagosome–lysosome fusion by ATG8 family members. *Curr. Biol.* **28**, R512–R518 (2018).
52. Wild, P., McEwan, D. G. & Dikic, I. The LC3 interactome at a glance. *J. Cell Sci.* **127**, 3–9 (2014).
53. Cullen, P. J. & Steinberg, F. To degrade or not to degrade: mechanisms and significance of endocytic recycling. *Nat. Rev. Mol. Cell Biol.* **19**, 679–696 (2018).
54. Lai, Z., Wang, F., Zheng, Z., Fan, B. & Chen, Z. A critical role of autophagy in plant resistance to necrotrophic fungal pathogens. *Plant J.* **66**, 953–968 (2011).
55. Geldner, N. et al. Rapid, combinatorial analysis of membrane compartments in intact plants with a multicolor marker set. *Plant J.* **59**, 169–178 (2009).
56. Yu, F., Park, S. & Rodermel, S. R. The *Arabidopsis* FtsH metalloprotease gene family: interchangeability of subunits in chloroplast oligomeric complexes. *Plant J.* **37**, 864–876 (2004).
57. Clough, S. J. & Bent, A. F. Floral dip: a simplified method for *Agrobacterium*-mediated transformation of *Arabidopsis thaliana*. *Plant J.* **16**, 735–743 (1998).
58. Lichtenthaler, H. K. [34] Chlorophylls and carotenoids: pigments of photosynthetic biomembranes. *Methods Enzymol.* **148**, 350–382 (1987).
59. Schägger, H. & von Jagow, G. Tricine-sodium dodecyl sulfate-polyacrylamide gel electrophoresis for the separation of proteins in the range from 1 to 100 kDa. *Anal. Biochem.* **166**, 368–379 (1987).
60. Zhuang, X. et al. A BAR-domain protein SH3P2, which binds to phosphatidylinositol 3-phosphate and ATG8, regulates autophagosome formation in *Arabidopsis*. *Plant Cell* **25**, 4596–4615 (2013).
61. Yoo, S.-D., Cho, Y.-H. & Sheen, J. *Arabidopsis* mesophyll protoplasts: a versatile cell system for transient gene expression analysis. *Nat. Protoc.* **2**, 1565–1572 (2007).

62. Schindelin, J. et al. Fiji: an open-source platform for biological-image analysis. *Nat. Methods* **9**, 676–682 (2012).
63. Avila, J. R., Lee, J. S. & Torii, K. U. Co-immunoprecipitation of membrane-bound receptors. *Arabidopsis Book* **13**, e0180 (2015).

Acknowledgements

This work was supported by grants from the National Natural Science Foundation of China (31570267 to F.Y., 31770205 to X.L. and 31741010 to Y.Q.) and Northwest A&F University (2452016001 to F.Y.). Y.W., L.S. and J.S. were supported by US National Institute of Health grant R01GM06493. We thank the Teaching and Research Core Facility at the College of Life Sciences, NWAFU for support in this work. We thank members of the Sheen Laboratory and K. Mao of Massachusetts General Hospital and Harvard Medical School, USA for stimulating discussions and critical reading of the manuscript.

Author contributions

X.L., J.Sheen and F.Y. conceived the study and designed the experiments. M.J., H.X, R.W., Y.C., N.X., J.Z., J.Shao and Y.Q. performed the experiments. M.J., X.L., Y.W., L.S. and L.A. analysed the data. M.J., X.L., J.Sheen and F.Y. wrote the manuscript with contributions from all authors.

Competing interests

The authors declare no competing interests.

Additional information

Supplementary information is available for this paper at https://doi.org/10.1038/s41477-018-0348-x.

Reprints and permissions information is available at www.nature.com/reprints.

Correspondence and requests for materials should be addressed to F.Y.

Publisher's note: Springer Nature remains neutral with regard to jurisdictional claims in published maps and institutional affiliations.

nature research

Corresponding author(s): Fei Yu

Reporting Summary

Nature Research wishes to improve the reproducibility of the work that we publish. This form provides structure for consistency and transparency in reporting. For further information on Nature Research policies, see Authors & Referees and the Editorial Policy Checklist.

Statistical parameters

When statistical analyses are reported, confirm that the following items are present in the relevant location (e.g. figure legend, table legend, main text, or Methods section).

n/a	Confirmed	
☐	☒	The exact sample size (*n*) for each experimental group/condition, given as a discrete number and unit of measurement
☐	☒	An indication of whether measurements were taken from distinct samples or whether the same sample was measured repeatedly
☐	☒	The statistical test(s) used AND whether they are one- or two-sided *Only common tests should be described solely by name; describe more complex techniques in the Methods section.*
☒	☐	A description of all covariates tested
☒	☐	A description of any assumptions or corrections, such as tests of normality and adjustment for multiple comparisons
☐	☒	A full description of the statistics including central tendency (e.g. means) or other basic estimates (e.g. regression coefficient) AND variation (e.g. standard deviation) or associated estimates of uncertainty (e.g. confidence intervals)
☐	☒	For null hypothesis testing, the test statistic (e.g. *F*, *t*, *r*) with confidence intervals, effect sizes, degrees of freedom and *P* value noted *Give P values as exact values whenever suitable.*
☒	☐	For Bayesian analysis, information on the choice of priors and Markov chain Monte Carlo settings
☒	☐	For hierarchical and complex designs, identification of the appropriate level for tests and full reporting of outcomes
☒	☐	Estimates of effect sizes (e.g. Cohen's *d*, Pearson's *r*), indicating how they were calculated
☐	☒	Clearly defined error bars *State explicitly what error bars represent (e.g. SD, SE, CI)*

Our web collection on statistics for biologists may be useful.

Software and code

Policy information about availability of computer code

Data collection	RT-qPCR data were acquired with the CFX Maestro Software (Bio-Rad). Confocal images were acquired with the IQ3.0 Imaging Workstation software (Andor). Fluorescent Images were acquired with the LAS X software (Leica).
Data analysis	Fiji-ImageJ was used to process images and measure fluorescence intensities. GraphPad Prism 7 was used to make graphs and perform statistical analyses. Clustal Omega (https://www.megasoftware.net/) was used to generate sequence alignments. iLIR (http://repeat.biol.ucy.ac.cy/cgibin/iLIR/iLIR_cgi) was used to predict AIMs.

For manuscripts utilizing custom algorithms or software that are central to the research but not yet described in published literature, software must be made available to editors/reviewers upon request. We strongly encourage code deposition in a community repository (e.g. GitHub). See the Nature Research guidelines for submitting code & software for further information.

Data

Policy information about availability of data

All manuscripts must include a data availability statement. This statement should provide the following information, where applicable:

- Accession codes, unique identifiers, or web links for publicly available datasets
- A list of figures that have associated raw data
- A description of any restrictions on data availability

Raw data of the findings presented in this study are available from the corresponding author upon request.

Field-specific reporting

Please select the best fit for your research. If you are not sure, read the appropriate sections before making your selection.

☒ Life sciences ☐ Behavioural & social sciences ☐ Ecological, evolutionary & environmental sciences

For a reference copy of the document with all sections, see nature.com/authors/policies/ReportingSummary-flat.pdf

Life sciences study design

All studies must disclose on these points even when the disclosure is negative.

Sample size	No statistical method was used to predetermine the sample sizes. All the experiments involving quantitative analyses were independently repeated at least three times. Sample sizes were judged as sufficient when results can be reliably reproduced. For qPCR analyses, three or four biological replicates were used. For chlorophyll and protein contents analyses, three biological replicates were used. Each biological replicate contained 10 randomly picked seedlings. For BiFC assay quantification, more than 90 cells from three independent sets of experiments were used. The exact number of analyzed cells for each BiFC plasmids pair was listed in the figures (Supplementary Fig. 5f and Supplementary Fig. 7e). To compare YFP-ARA7 and ABS3-GFP fluorescence intensities, more than 30 swollen MVBs from two seedlings of each fluorescent line were measured. The exact number of analyzed MVBs in each genotype was listed in the figure legend (Supplementary Fig. 2g). For cathepsin B protease activity estimation, Magic Red fluorescence intensities from more than 450 cells of each genotype were measured. The exact number of analyzed cells was listed in the figure legend (Supplementary Fig. 2i).
Data exclusions	No data were excluded.
Replication	The experimental findings were reliably reproduced at least three times in this study.
Randomization	All samples were collected randomly.
Blinding	Genotypes or the combination of plasmids were not known a priori when the confocal imaging experiments were carried out.

Reporting for specific materials, systems and methods

Materials & experimental systems

n/a	Involved in the study
☐	☒ Unique biological materials
☐	☒ Antibodies
☒	☐ Eukaryotic cell lines
☒	☐ Palaeontology
☒	☐ Animals and other organisms
☒	☐ Human research participants

Methods

n/a	Involved in the study
☒	☐ ChIP-seq
☒	☐ Flow cytometry
☒	☐ MRI-based neuroimaging

Unique biological materials

Policy information about availability of materials

Obtaining unique materials	Unique materials generated in this study are available from the corresponding author upon request.

Antibodies

Antibodies used

Polyclonal anti-ATG8 (1:1000 dilution) was prepared in house following the procedures described in Zhuang et al. (2013). Other antibodies used in this study are commercially available (anti-NBR1, AS142805, Agrisera, 1:4000 dilution; anti-RBCL AS03037, Agrisera, 1:20000 dilution; anti-PBA1, ab98861, abcam, 1:1000 dilution; monoclonal anti-GFP, JL-8 clone, 632381, Takara, 1:2500 dilution).

Validation

anti-ATG8, Zhuang, X. et al. (2013). A BAR-domain protein SH3P2, which binds to phosphatidylinositol 3-phosphate and ATG8, regulates autophagosome formation in Arabidopsis. Plant Cell. 25, 4596-4615.
Validation statement for anti-NBR1 can be found at the product website <https://www.agrisera.com/en/artiklar/nbr1.html>.
Validation statement for anti-RBCL can be found at the product website <https://www.agrisera.com/en/artiklar/rbcl-rubisco-large-subunit-form-i-and-form-iiplastid-stroma-global-antibody.html>.
Validation statement for anti-PBA1 can be found at the product website <https://www.abcam.com/pba1-antibody-ab98861.html#top-0>.
Validation statement for monoclonal anti-GFP can be found at the product website <https://www.takarabio.com/products/antibodies-and-elisa/fluorescent-protein-antibodies/green-fluorescent-protein-antibodies?catalog=632475>.